



# Total Control

*Advanced integrated supervisory and wind turbine control  
for optimal operation of large Wind Power Plants*

Validation of high-fidelity models against  
Lillgrund wind-field and load data

D1.2

Delivery date: 25-01-2022

Lead beneficiary: KU Leuven

Dissemination level: Public



This project has received funding  
from the European Union's Horizon  
2020 Research and Innovation  
Programme under grant agreement  
No. 727680

Author(s) information (alphabetical):		
Name	Organisation	Email
Søren Juhl Andersen	DTU	<a href="mailto:sjan@dtu.dk">sjan@dtu.dk</a>
Valentin Bernard	SWP	<a href="mailto:valentin.bernard@siemensgamesa.com">valentin.bernard@siemensgamesa.com</a>
Laurent Beaudet	SWP	<a href="mailto:laurent.beaudet@siemensgamesa.com">laurent.beaudet@siemensgamesa.com</a>
Louis Da Costa	SWP	<a href="mailto:louis.da@siemensgamesa.com">louis.da@siemensgamesa.com</a>
Paul Deglaire	SWP	<a href="mailto:paul.deglaire@siemensgamesa.com">paul.deglaire@siemensgamesa.com</a>
Johan Meyers	KUL	<a href="mailto:johan.meyers@kuleuven.be">johan.meyers@kuleuven.be</a>
Ishaan Sood	KUL	<a href="mailto:ishaan.sood@kuleuven.be">ishaan.sood@kuleuven.be</a>
Niels Troldborg	DTU	<a href="mailto:niet@dtu.dk">niet@dtu.dk</a>

#### Document information

Version	Date	Description	Prepared by	Reviewed by	Approved by
1	12.10.2021	Ishaan Sood, Valentin Bernard, Laurent Beaudet, Louis Da Costa, Paul Deglaire, Søren Juhl Andersen, Niels Troldborg		Johan Meyers	Gunner Chr. Larsen
2	24.11.2021	Ishaan Sood, Søren Juhl Andersen		Johan Meyers	Gunner Chr. Larsen

# TABLE OF CONTENTS

Table of Contents .....	3
Introduction.....	4
A. Lillgrund Wind Power Plant .....	4
B. Validation of numerical models .....	6
B.1. Simulation platforms .....	6
B.1.1. SP-Wind (KU Leuven) .....	6
B.1.2. EllipSys-3D (DTU) .....	8
B.2. Validation cases .....	8
B.2.1. SP-Wind .....	8
B.2.2. EllipSys-3D .....	10
B.3. Results .....	10
B.3.1. SP-Wind .....	10
B.3.2. EllipSys-3D .....	12
C. Validation of DWM model .....	14
C.1. DWM-LiDAR Comparison .....	14
C.1.1. Overview .....	14
C.1.2. Analysis of the data .....	15
C.1.3. Results.....	15
C.2. A new approach of dwm.....	16
C.2.1. An alternative wake superposition assumption .....	16
C.2.2. Results.....	16
C.2.3. Conclusion .....	17
D. Conclusions and Discussion .....	17
E. REFERENCES .....	18
Annex.....	19

## INTRODUCTION

Recent years have seen the emergence of windfarm simulation models that cover the whole chain from a flow coupled aero-elastic model to a power-grid model. These tools have led to the discovery of coordinated windfarm control strategies for the purposes of power maximization, asset life extension and grid frequency regulation. However, validation of these numerical models and strategies requires accurate reference data. Detailed field measurements under controlled conditions from existing windfarms which consist of flow field and loading measurements can thus be used to validate such numerical tools.

As part of the TotalControl project, a measurement campaign was carried out at the Lillgrund windfarm, located 10 km off the coast of southern Sweden. The high-resolution flow field measurement campaign made use of three long-range LiDAR's to resolve the flow field in a plane, which covers a substantial part of the Wind Power Plant (WPP) field. The flow field measurements were supplemented by simultaneous power measurements from the individual wind turbines. Thus, the resulting database provides a valuable asset for comparing and validating numerical modelling tools.

The current report is composed of 2 studies. The first one discusses the validation of high-fidelity numerical models against data from the Lillgrund wind farm. Findings from coupled flow and aeroelastic solvers such as SP-WIND (KU Leuven) and EllipSys3D/Flex5 (DTU) are compared against measurements from the Lillgrund windfarm for validation. Comparison is made on the basis of accurate representation of the windfarm power production, turbine loading across the windfarm, and the wake deficit. The second study shows the ability of the mid-fidelity Siemens Gamesa DWM model to reproduce turbine wakes. More precisely, this study defines at which distance downstream the wake-inducing turbine the DWM model characterizes the velocity field correctly by comparing to LiDAR measurements. As the turbines of interest are in the middle of the farm, different methods of superposition are tested during this study.

The document is outlined as follows. First, a brief review of the Lillgrund windfarm and results from the measurement campaign are given in section A. Then, the first study is presented in section B, where sub-section 1 details the different numerical tools and setups, sub-section 2 outlines the selected simulation cases for validation and finally the results are presented in sub-section 3. The second study is presented in section C, where sub-section 1 gives an explanation on how the DWM-LiDAR comparison has been done and shows first results, and section 2 describes two alternative ways of using DWM and compares the results obtained with the various methods of DWM. Finally, a brief conclusion highlighting the strengths and weaknesses of the different models used in this report is presented in section D.

## A. LILLGRUND WIND POWER PLANT

Lillgrund Wind Farm is located about 10 km off the coast of southern Sweden, just south of the Øresund Bridge, where average wind speeds are 8 to 10 metres per second. The windfarm has 48 wind turbines (Siemens SWT-2.3-93) and a capacity of 110 megawatts (MW). The farm's turbines have a rotor diameter of 93 metres and a total height of 115 metres. Three long-range LiDAR's to resolve the flow field in a plane, which covers a substantial part of the WPP field as shown in Figure 1. Wind speed and direction measurement data at the hub height of the Lillgrund wind turbines can be seen in Figure 2. Loading data is also available for 6 turbines: B06, B07, B08, C08, D07, D08; spanning the duration of the measurement campaign.

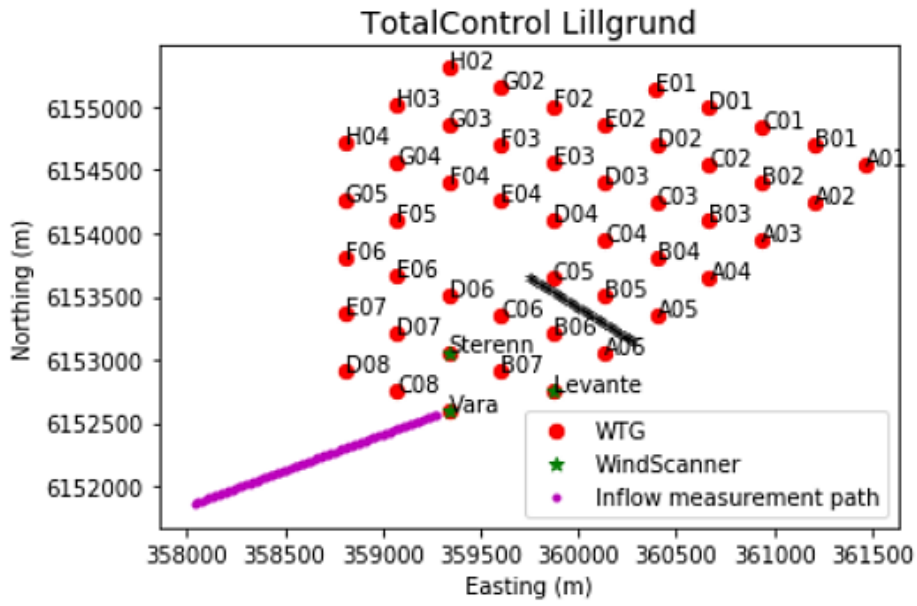


Figure 1 Lillgrund windfarm layout comprising of 48 Siemens 2.3 MW turbines. The pink line shows the range gate locations along the LIDAR inflow measurement path

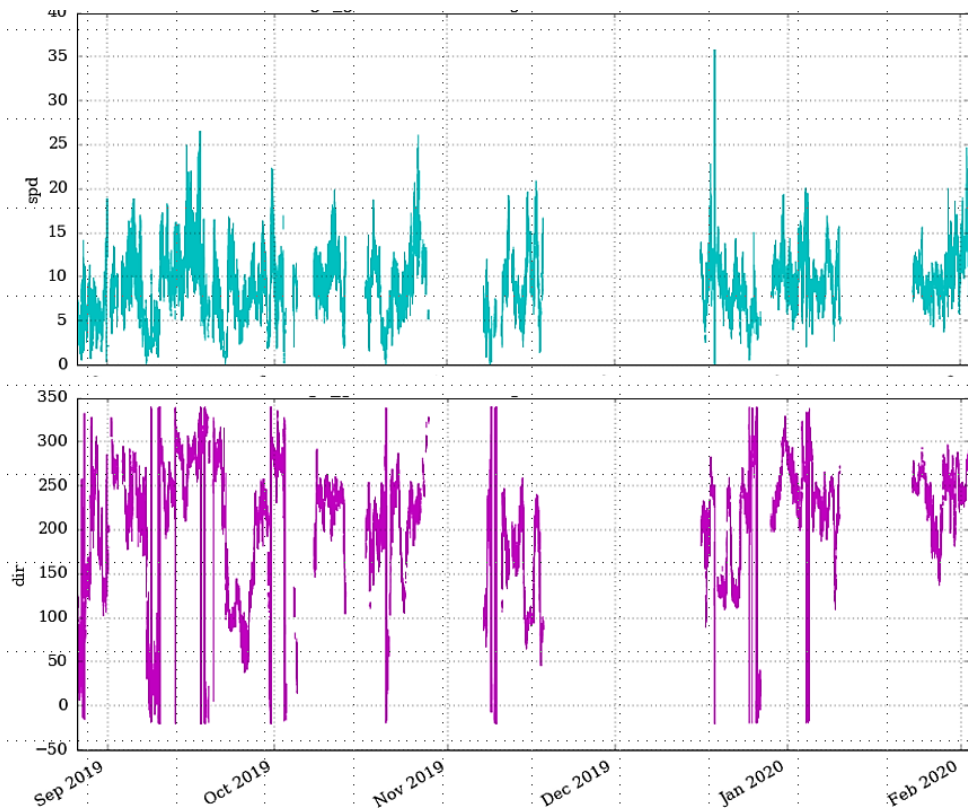


Figure 2 Wind speed and direction time series at hub height. Missing data corresponds to equipment downtime and failure

## B. VALIDATION OF NUMERICAL MODELS

### B.1. SIMULATION PLATFORMS

This section details the coupled flow and aeroelastic solvers used for validation against the measurement data. Simulations are performed by KU Leuven (using SP-Wind) and DTU (using EllipSys3D). A short description of these simulation platforms is given below.

#### B.1.1. SP-WIND (KU LEUVEN)

SP-Wind is a wind-farm Large Eddy Simulation code built on a high-order flow solver developed over the last 10 years at KU Leuven (Allaerts and Meyers, 2015; Goit and Meyers, 2015; Munters and Meyers, 2018). The three-dimensional, unsteady, and spatially filtered Navier-Stokes momentum and temperature equations

$$\begin{aligned} \frac{\partial \tilde{\mathbf{u}}}{\partial t} + (\tilde{\mathbf{u}} \cdot \nabla) \tilde{\mathbf{u}} &= -\frac{\nabla(\tilde{p} + p_\infty)}{\rho} - \nabla \cdot \boldsymbol{\tau}_s + 2\boldsymbol{\Omega} \times \tilde{\mathbf{u}} + \mathbf{g}(\tilde{\theta} - \theta_0)/\theta_0 + \boldsymbol{\tau}_w + \mathbf{f} \\ \frac{\partial \tilde{\theta}}{\partial t} + (\tilde{\mathbf{u}} \cdot \nabla) \tilde{\theta} &= -\nabla \cdot \mathbf{q}_s \end{aligned}$$

are solved by means of Large-Eddy Simulations. In these equations,  $\tilde{\mathbf{u}}$  and  $\tilde{p}$  are the filtered velocity and pressure fields respectively. Further,  $\tilde{\theta}$  is the filtered potential temperature field, and  $\theta_0$  is the background adiabatic base state. The pressure gradient is readily split into a background pressure gradient  $\nabla p_\infty$  driving the mean flow, and a fluctuating component  $\nabla \tilde{p}$ . The very high Reynolds numbers in atmospheric boundary-layer flows combined with typical spatial resolutions in LES justify the omission of resolved effects of viscous momentum transfer and diffusive heat transfer. Instead, these are represented by modeling the subgrid-scale stress tensor  $\boldsymbol{\tau}_s$  and the subgrid-scale heat flux  $\mathbf{q}_s$  originating from spatially filtering the original governing equations. Coriolis effects are included through the Earth's angular velocity vector  $\boldsymbol{\Omega}$ , and thermal buoyancy is represented by  $\mathbf{g}(\theta - \theta_0)/\theta_0$ , with  $\mathbf{g}$  the gravitational acceleration  $\tilde{\theta}$  the filtered potential temperature and  $\theta_0$  a reference temperature. The effect of the sea surface is included using a rough-wall stress boundary  $\boldsymbol{\tau}_w$ , corresponding to a logarithmic velocity profile with a roughness length  $z_0$ . Finally,  $\mathbf{f}$  represents any remaining body forces (e.g. by wind turbines) on the flow. Spatial discretization is performed by combining pseudo-spectral schemes with fourth-order energy-conservative finite differences. The equations are marched in time using a fully explicit fourth-order Runge-Kutta scheme, and grid partitioning is achieved through a scalable pencil decomposition approach. Subgrid-scale stresses are modeled with a standard Smagorinsky model with wall damping. The subgrid-scale heat flux is calculated from the resolved potential temperature profile using an eddy-diffusivity model. The Siemens 2.3 MW turbines are modeled by an actuator sector (AS) model, coupled with a nonlinear flexible multi-body dynamics model (Vitsas and Meyers, 2016). Turbines are controlled using an implementation of the DTU wind energy controller (Hansen et al. 2013).

The turbulent inflow conditions for windfarm inflow are obtained from the precursor data from the Totalcontrol Flow database (Anderson et al., 2020). The precursor data contains unsteady three-dimensional flow data of an unperturbed atmospheric boundary layer (i.e. without the influence of turbines). The database comprises of pressure driven and conventionally neutral boundary layers, spanning different surface roughness lengths and boundary layer heights. A streamwise slab of the velocity and temperature field is stored to disk when running the precursor, and is later introduced in the wind-farm domain by means of body forces in a so-called fringe region (Munters et al., 2016).

To match the inflow conditions measured by the LIDAR measurement campaign, the data from the precursor dataset can be transformed to different flow conditions by rescaling the flow variables by the correct scaling parameters. Firstly, it is well known that the appropriate velocity scaling is the friction velocity  $u_*$ , and hence different wind speeds can be attained by rescaling the entire flow field by a different friction velocity  $u_*^{new}$ . Second, for rough-wall boundary layers at high Reynolds numbers in which the roughness elements are much smaller than the boundary-layer height (it is the case for offshore atmospheric boundary layers), the roughness acts merely to increase surface stress without any structural changes in the flow (Castro, 2007; Jiménez, 2004), in line with the classical outer layer similarity hypothesis (Townsend, 1976). The effect of a different roughness length  $z_0^{new}$  can thus be captured by imposing an offset on the mean flow in line with the difference in roughness. Hence, denoting the imposed friction velocity and roughness length in the current cases by  $u_*^{old}$  and  $z_0^{old}$  respectively, the flow can be rescaled and shifted as

$$\mathbf{u}^{new}(x, t) = u_*^{new} \left[ \frac{\mathbf{u}^{old}(x, t)}{u_*^{old}} + \frac{1}{\kappa} \ln \frac{z_0^{old}}{z_0^{new}} \right],$$

Where  $\kappa$  is the von Kármán constant.

Similarly, the effect of rescaling the flow field by a new friction velocity on the time-step can be determined by

$$\Delta t^{new} = \frac{\Delta t}{u_*^{new}} u_*$$

The simulation domain has a size of  $16 \times 16 \times 1.5 \text{ km}^3$  in the streamwise, spanwise, and vertical directions respectively. The grid resolution is  $13.33 \times 13.33 \times 6.66 \text{ m}^3$ , resulting in a computational grid of  $1200 \times 1200 \times 225 = 324 \times 10^6$  gridpoints. Wind-farm simulations are performed in a sequence of steps. First, a fully-developed turbulent boundary layer is generated in a so-called *spinup* simulation with periodic boundary conditions but without turbines. Profiles of the available precursor data are shown in Figure 3 and Figure 4, and further details of the spinup simulations to generate the precursor data can be found in the TotalControl report (Anderson et al., 2020). The data from the precursor simulations can be fed as inflow conditions to a set of wind-farm configurations. The flow is then allowed to pass through the wind farm for 15 minutes to account for start-up transients, after which data collection and computation of flow statistics is done. The wind farm simulations are run for a time period of 90 minutes. The SP-Wind simulations has a LES time step of 0.5 second, while the aero-elastic computations are performed with a smaller time step of 0.01 seconds. The general domain and time parameters are summarized in Table 1.

Table 1 SP- Wind domain parameters

Domain size	$L_x \times L_y \times L_z$	$16 \times 16 \times 1.5 \text{ km}^3$
Grid	$N_x \times N_y \times N_z$	$1200 \times 1200 \times 225$
Resolution	$\Delta_x \times \Delta_y \times \Delta_z$	$13.33 \times 13.33 \times 6.66 \text{ m}^3$
Wind farm spinup time	$T_{spin}$	15 min
Simulation time	$T$	75 min
LES Time step	$\Delta t_{LES}$	0.5 s
Structural time step	$\Delta t_{struct}$	0.01 s

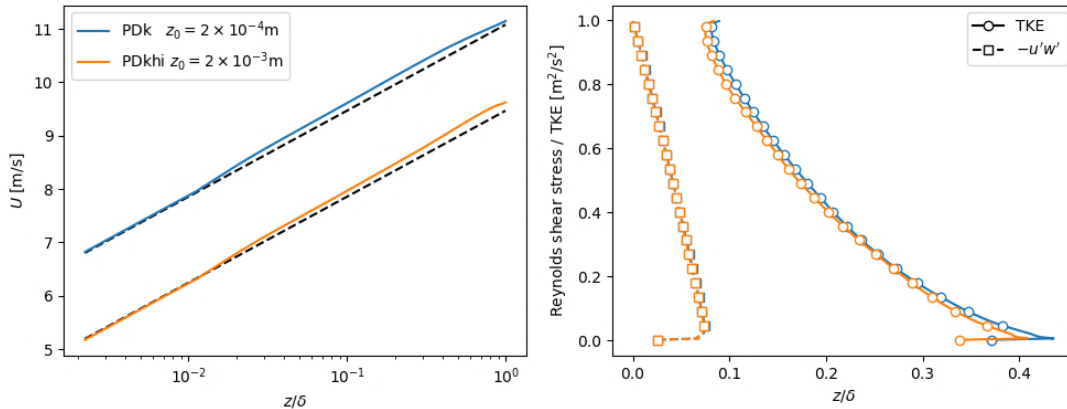


Figure 3 Flow profiles for PDBL cases of KU Leuven. Left: Mean velocity. Dashed lines indicate log-law profiles. Right: resolved Reynolds shear stress and turbulent kinetic energy

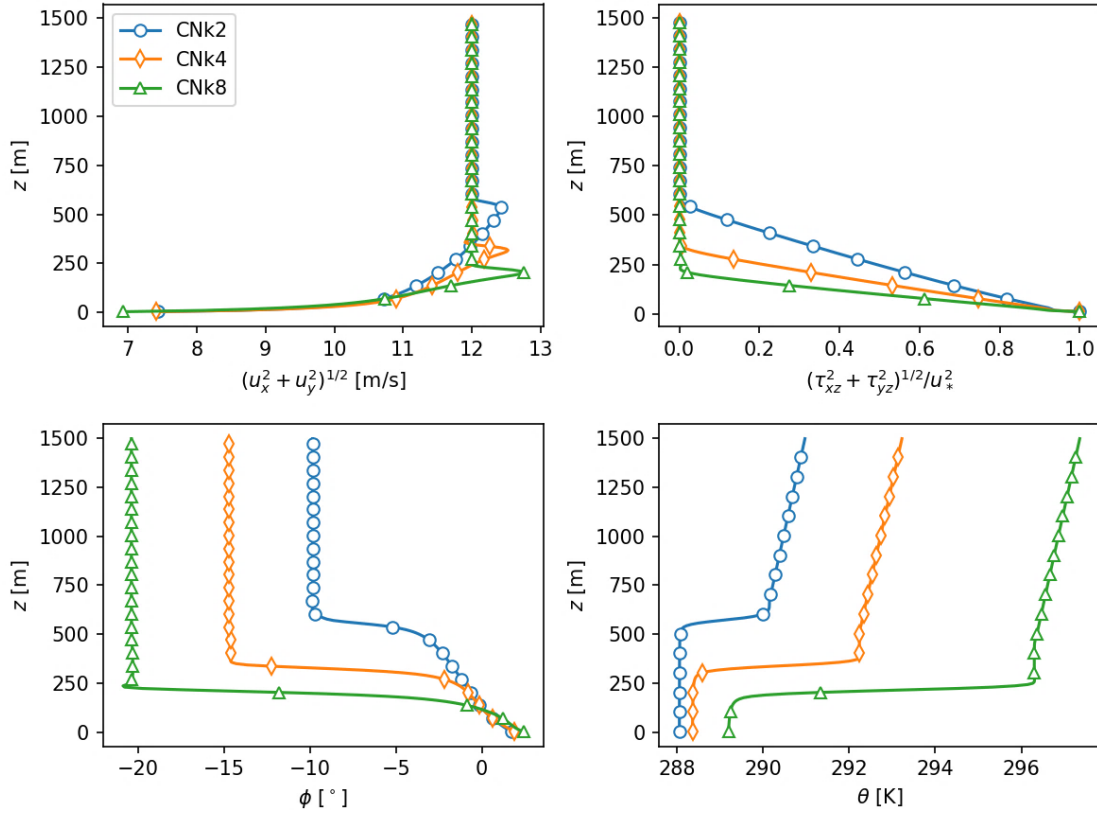


Figure 4 Flow profiles for KU Leuven CNBL cases with varying boundary layer heights. Top left: Horizontal Velocity. Top right: Total (Resolved + Subgrid) shear stress. Bottom left: Wind veer. Bottom right: Potential temperature

### B.1.2. ELLIPSYS-3D (DTU)

EllipSys3D is a general-purpose flow solver (Michelsen 1992, Sørensen 1994), solving the discretized incompressible Navier – Stokes equations in general curvilinear coordinates using a block-structured finite-volume approach. Pressure coupling is achieved using the SIMPLE algorithm with Rhie-Chow momentum interpolation. The convective terms are discretized using the fourth order central difference scheme. The subgrid-scale stresses are modeled with Deardorff model. The turbines are modeled using the actuator disc/sector (AS) method (Mikkelsen 2004), which has been fully coupled to the aero-elastic tool, Flex5 (Øye 1996). Turbulent inflow is also generated in separate precursor simulations, where the velocities are extracted at a given plane in the domain and saved for later use. These will be introduced directly on the inflow boundary in the simulations of wind-farms.

## B.2. VALIDATION CASES

As the LIDAR measurement campaign spanned several months, selection of viable subsets of the measured data for comparison was an important challenge, which was mainly governed by the capabilities and limitations of the solvers. This section details the methodology of selecting the validation cases for each solver and the associated results.

### B.2.1. SP-WIND

While SP-Wind does support changing wind directions during a simulation run (Munters et al., 2016), each simulation is restricted to a single wind direction and a time frame of 75 mins to limit computational costs. Thus, the available data from the measurement campaign was divided into numerous 75 minutes overlapping time windows, and filtered for minimal variation in wind direction. In each time window, two distance metrics are used to determine the similarity between the LIDAR data from the measurement campaign and the 5 available flow datasets from the TotalControl LES database. These metrics are defined as,

$$d_1 = \sqrt{\sum w_i (\bar{x}_{A_i} - \bar{x}_{B_i})^2}, \quad d_2 = \sqrt{\sum \sum w_i (\sigma_{A_{ij}} - \sigma_{B_{ij}})^2}.$$

Where,  $\mathbf{A}$  is the lidar data set,  $\mathbf{B}$  is an inflow from LES dataset,  $\mathbf{i}$  is the range gate location and  $\mathbf{j}$  is the time index. As per their definitions,  $d_1$  provides a measure of the difference between the vertical mean profiles, while  $d_2$  is a difference

between the covariances of the two datasets, accounting for spatial variations. The available LES datasets can further be generalized and expanded by using the scaling parameters  $u_*^{new}$  and  $z_0^{new}$ , as outlined in section B 1.1, to obtain new flow realizations. Therefore, an optimization problem can be solved which sweeps over the entire lidar measurement campaign to determine the time windows over which each LES dataset is the most similar to the available LIDAR data. The distance metrics are also assigned weights, giving preferences to range gates spanning the rotor plane.

$$\min J(A, B) = d_1 + d_2$$

Based on the outputs of the optimization problem, 5 unique time windows of 75 minute length each, corresponding to 5 different LES flow realizations which best matched the LIDAR data are chosen. 3 of these matches are obtained by transforming the PDK TotalControl LES dataset, while the 4<sup>th</sup> and 5<sup>th</sup> matches are obtained directly from the CNk4 and CNk8 datasets respectively. A comparison of the mean vertical profiles at range gate location for these cases are shown in Figure 5, and their details are summarized in Table 2.

Table 2 Specifications of selected validation cases

Simulation	Measurement campaign time	Friction Velocity $u_*$	Surface Roughness $z_0$	Hub height direction $\theta$	Hub height velocity $v_h$
PDK <sub>1</sub>	2019-12-23, T01:14:44	0.26 m/s	$5.6 \times 10^{-4} m$	119°	8 m/s
PDK <sub>2</sub>	2019-12-18, T18:48:04	0.28 m/s	$2 \times 10^{-4} m$	243°	8.5 m/s
PDK <sub>3</sub>	2019-09-24, T18:01:46	0.17 m/s	$1.8 \times 10^{-5} m$	110°	4.5 m/s
CNk4 <sub>1</sub>	2020-01-29, T05:40:36	0.28 m/s	$2 \times 10^{-4} m$	251°	10.5 m/s
CNk8 <sub>1</sub>	2020-01-07, T17:46:26	0.28 m/s	$2 \times 10^{-4} m$	222°	10.5 m/s

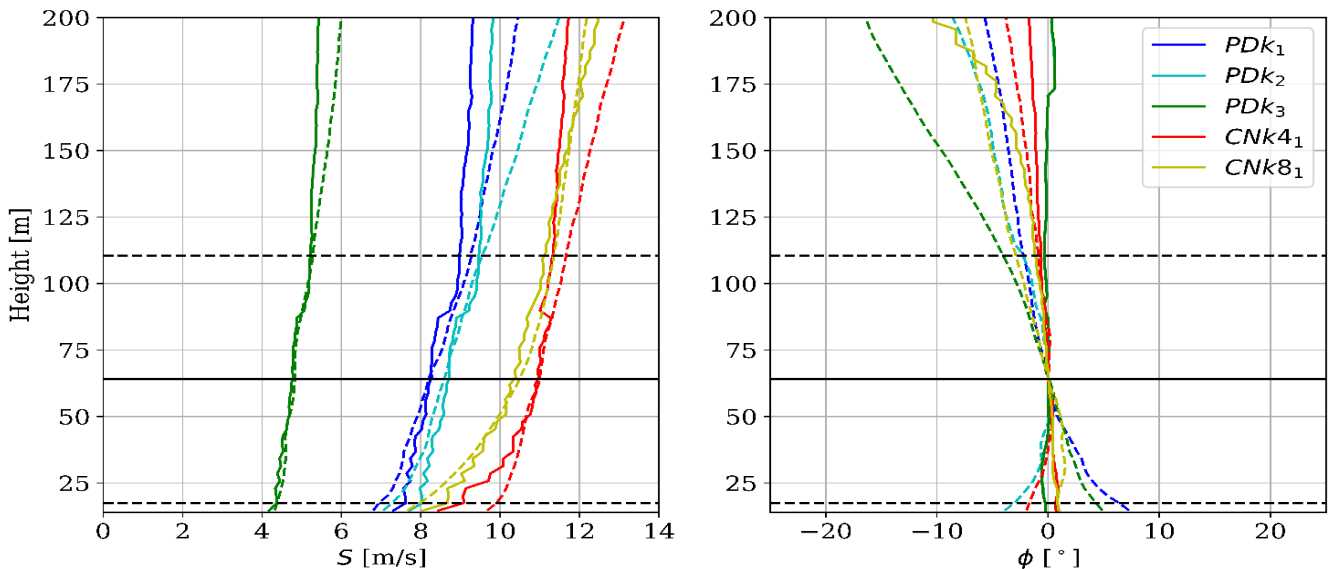


Figure 5 Comparison of vertical mean total velocity profile (left) and wind veer (right) between the selected LES and corresponding LIDAR data. Solid lines represent the LES data and dashed lines of the same colour represent the LIDAR data. Solid and dashed black

From Figure 5, it can be seen that all the selected LES cases match the LIDAR measurements very well across the rotor area. Larger deviations can be observed at heights above the rotor tip, which can be attributed to the preference given to the rotor disc area when finding the best matches in the optimization problem. While the PDBL simulations have a larger error when comparing the veer between the LES and LIDAR measurements (as by definition, the PDBL simulations have zero veer), the absolute error never exceeds more than 7 degrees over the rotor area for any of the cases.

### B.2.2. ELLIPSYS-3D

Based on the above analysis, a precursor corresponding to PDK<sub>2</sub> has also been performed and rescaled in order to perform simulations PDK<sub>1-3</sub>. Figure 6 shows a comparison between LES and the LIDAR measurements. The EllipSys LES is in very good agreement with the expected logarithmic law of the wall and fits the LIDAR data fairly well especially across the rotor area. Above the top of the rotor tip there are large deviations as also observed and explained in the previous section. Overall, the EllipSys LES obtains an agreement with the LIDAR measurements which is comparable to that obtained with SP-Wind.

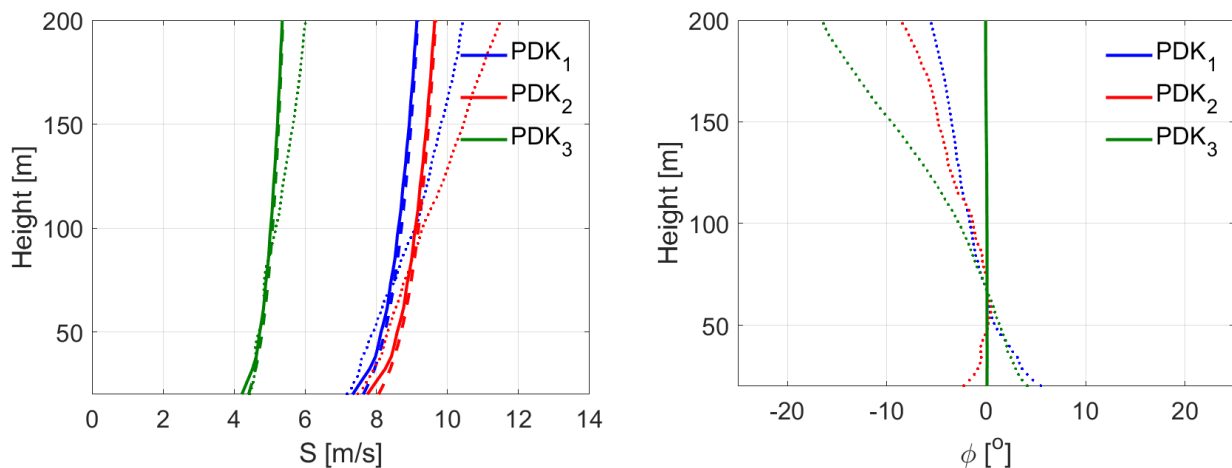


Figure 6 Comparison of vertical mean total velocity profile (left) and wind veer (right) between EllipSys LES and the corresponding LIDAR data. Solid lines represent the LES data, dots of the same colour represent the LIDAR data and dashed lines the theoretical

## B.3. RESULTS

This section presents a comparison between field measurements and the results obtained using the different numerical codes presented in this report, for the selected validation cases outlined in Section B2. For each simulation tool, performance is evaluated on the basis of comparing the power production of all the turbines within the farm, the wakes behind a sub-set of the turbines and the blade root bending moments for the turbines whose loading measurements are available during the campaign.

### B.3.1. SP-WIND

Comparison of the wind farm power output obtained from SP-Wind against the field measurements from Lillgrund is presented in Figure 7. For all the selected validation cases, good comparison is observed in both the individual wind turbine power output and total wind farm power production. Individual turbine power trends show good agreement with field data, accurately capturing the trends for power peaks and valleys for un-waked and waked turbines, indicating that the wind direction in the LES cases matches the real world field conditions during the time windows. Minor discrepancies can be observed in the trends, which can be attributed to the fact that while all the turbines in the simulation domain of SP-Wind are aligned with the wind, this may not be the case for the field measurements, resulting in minor errors due to yaw misalignment. Of all the simulated cases, only the PDK<sub>3</sub> has considerable error in power generation. This could be attributed to the low hub height wind speed of 4.5 m/s for this case, which causes the downstream waked turbines at the Lillgrund windfarm to shut down for majority of the time window duration as the wind speed falls below the start-up speed. This does not seem to occur in SP-Wind due to a controller mismatch, leading to higher power prediction in the LES simulation than the field measurements.

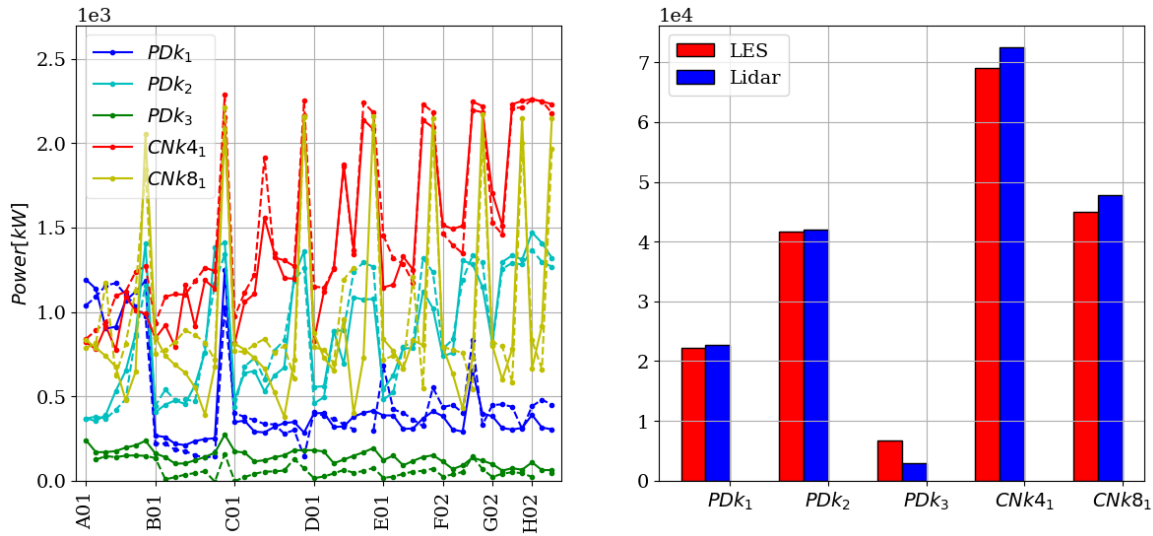


Figure 7 Comparison of LES time averaged power output of individual turbines (left) and total wind farm power output (right) against field measurements. Solid lines represent the LES data and dashed lines of the same colour represent the field data.

Comparison of the flapwise blade root bending moments for 6 turbines from the Lillgrund windfarm are shown in Figure 8 and Figure 9. To determine the effect of fatigue, we use the damage equivalent loads (DELs) to compare the load histories of the same turbine across the LES and field measurement data. DEL is computed using the Palmgren-Miner rule and the Wöhler equation to account for accumulating fatigue damage caused to the wind turbine components by the fluctuating structural loads (Sutherland, 1999). The loads time series are counted and binned into individual cycles using the rainflow-counting algorithm (Socie and Downing, 1982), and for the wind turbine blades the components follow the Wöhler’s curve with a slope coefficient equal to 10 (Freebury and Musial, 2000). DEL analysis is conducted only for the PDBL cases, as the time series data from the CNBL simulations had missing instances, making them unfit for rainflow analysis. For both the average blade root flapwise moments and the corresponding DELs, good comparison is obtained for most of the turbines for both the PDBL and CNBL cases. Error bars are included as 95% confidence intervals, evaluated using the block bootstrap method with 10,000 iterations. The source of error could be attributed to a combination of yaw error and the controller mis-match. For all the simulations, it can be observed that larger errors are reported for the turbines operating a waked state, eg. Bo6 and Bo7, while the predictions for the upstream turbines are in good agreement with the measurements. This could exhibit a shortcoming of the flow solver, whose lower grid resolution is unable to capture the small high turbulent structures in the wind turbine wakes, leading to incorrect loading predictions for waked turbines.

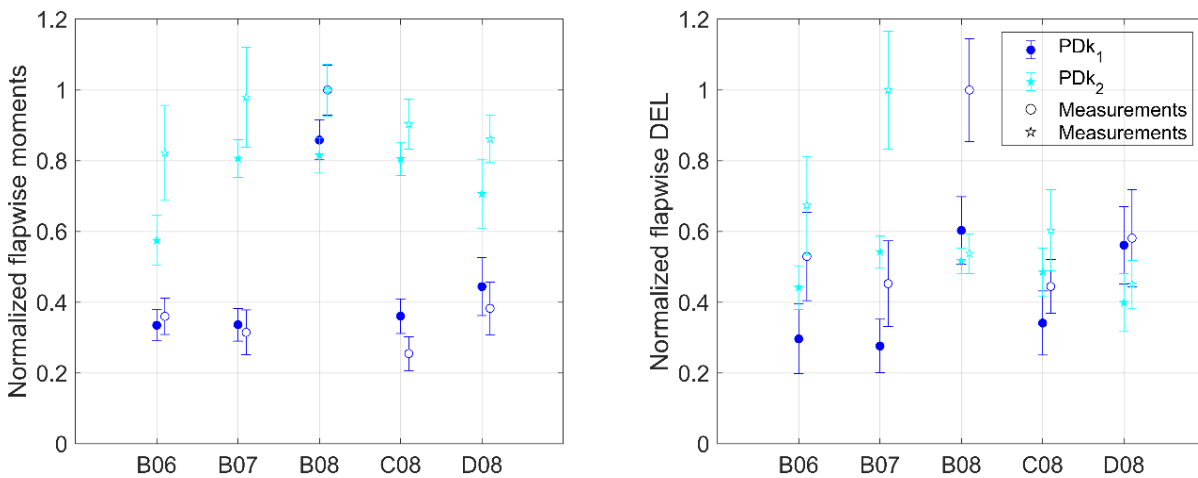


Figure 8 Comparison of LES time averaged blade root flapwise moments (left) and DEL (right) against field measurements for the PDBL simulations. Solid lines represent the LES data and dashed lines of the same colour represent the field data. Vertical lines represent 95% confidence intervals, obtained using the block bootstrap method.

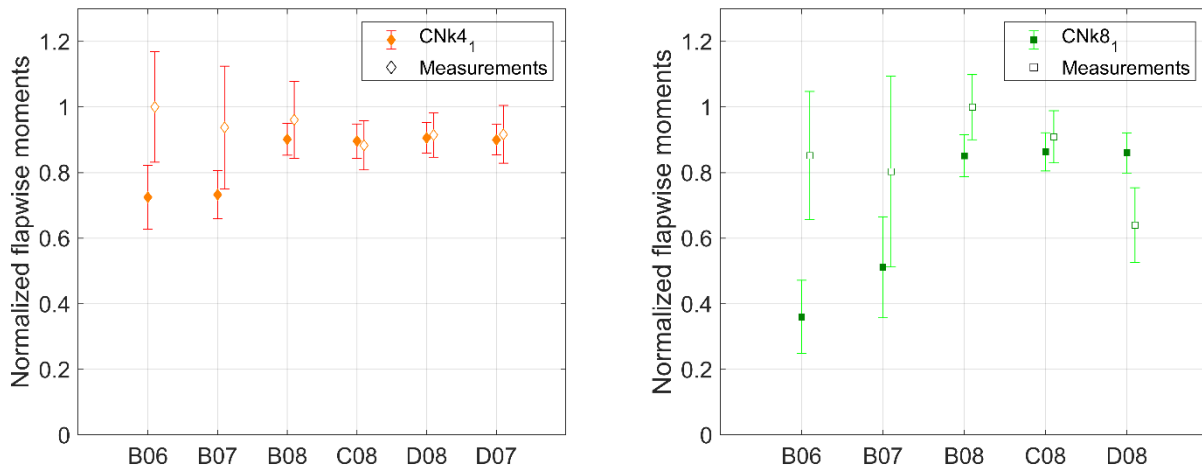


Figure 9 Comparison of LES time averaged blade root flapwise moments for the CNBL simulations.

Figure 10 shows a comparison of time averaged measurements obtained from the wake LIDARs placed within the Lillgrund windfarm against the results from the numerical models for two of the 5 validation cases. Data for the remaining 3 cases was not available due to equipment failure. For the CNk<sub>4</sub> case, good comparison can be seen for both the time averaged velocity field at hub-height, as well as the wake deficit behind turbine B06. It can be observed that while the nearwake predictions behind turbine B06 have a good comparison, SP-Wind overestimates the wake deficit in the far downstream region of 4D, leading to lower reported power production of the downstream turbine as seen in Figure 7. Larger errors can be seen for the PDK<sub>3</sub> case due to incorrectly estimating the wind direction, which also corresponds to the larger errors seen in the power production in Figure 7.

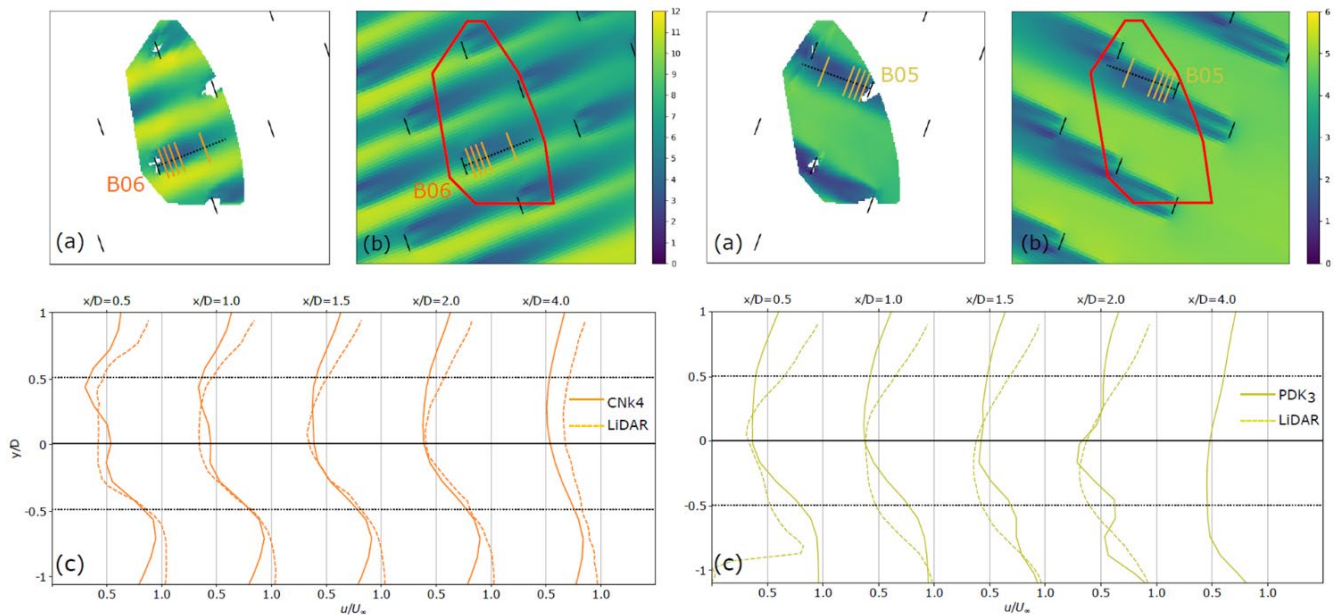


Figure 10 Hub-height flow field comparison between LES and wake LIDAR measurements for the case CNk<sub>4</sub> (left) and PDK<sub>3</sub> (right). a) LIDAR measurements b) LES measurements c) Wake deficit analysis

### B.3.2. ELLIPSYS-3D

Figure 11 shows the power predictions of EllipSys3D compared to the measurements from Lillgrund during PDK<sub>1-3</sub>. The left shows the mean power production of the 48 turbines, where the model results are in full lines, while the dashed lines show the measurements. Generally, the trends of the model results match the measurements well indicating that the peaks and valleys for unwaked and waked turbines are captured correctly. Some discrepancies arise occasionally. For instance for PDK<sub>1</sub> where the turbines (e.g. 31 and 40 corresponding to Eo1 and Fo5) on the edge of the farm or immediately after the recovery hole in the wind farm produce significantly more in the measurements. However, the

absolute level is underestimated by EllipSys3D for PDK<sub>1-2</sub>, while it is overestimated for PDK<sub>3</sub>. As for SP-Wind, the discrepancies can be due to differences in the simulated inflow, unintentional yaw misalignment and/or controller implementation. It is unclear why the predictions of EllipSys3D deviates more from the measurements than SP-Wind, but is most likely due to differences in the rotor force smearing and tip correction method. At least the differences cannot be explained from differences in the inflow, which are quite similar as is evident from Figure 5 and 6. The total power production of Lillgrund wind farm is shown on the right. The same trend is observed that the predicted power is underestimated for PDK<sub>1-2</sub>, while it is overestimated for PDK<sub>3</sub>. Scenario PDK<sub>1</sub> has been run for two different mesh resolutions of 9.3m and 4.65m in the horizontal and vertical direction around the turbines, corresponding to 5 and 10 cells per radius. The grid dependency is clear, as the predicted total power production decrease for increased resolution. This is a well-known effect as e.g. shown by Martinez-Tossas et al. (2015).

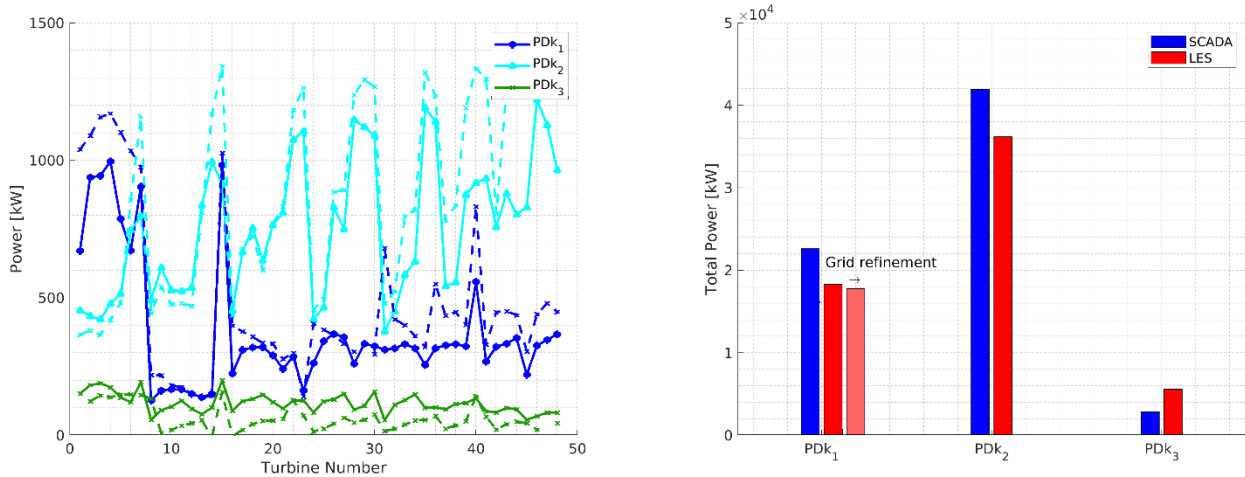


Figure 11 Comparison of EllipSys3D LES time averaged power output of individual turbines (left) and total wind farm power output (right) against field measurements. Solid lines represent the LES data and dashed lines of the same colour represent the field data. Light red on (right) show results from a refined simulation.

The normalized flapwise root bending moments of 5 turbines in the Lillgrund wind farm are shown in Figure 12. The left panel shows the normalized mean flapwise bending moment, while the right shows the normalized damage equivalent loads (DEL). The model estimates are again in full lines, while dashed lines show the measurements. Additionally, +/- one standard deviation is added, and the lines are slightly offset in the horizontal for clarity. The trends of the mean flapwise root bending moments are very well captured by the model as the loads peaks at turbine Bo8, and the model and measurements always overlap within one normalized standard deviation. However, it should be mentioned that we observe quite large deviations in the absolute value of the bending moments for PDK<sub>2</sub>, which is as expected due to the difference in absolute power production. It is noteworthy, how the standard deviation of the mean flapwise root bending moments of the model estimates are occasionally larger than those of the experiments, particular for turbines Co8 and Do8. The overall trends are captured very well for the DEL with the model predictions.

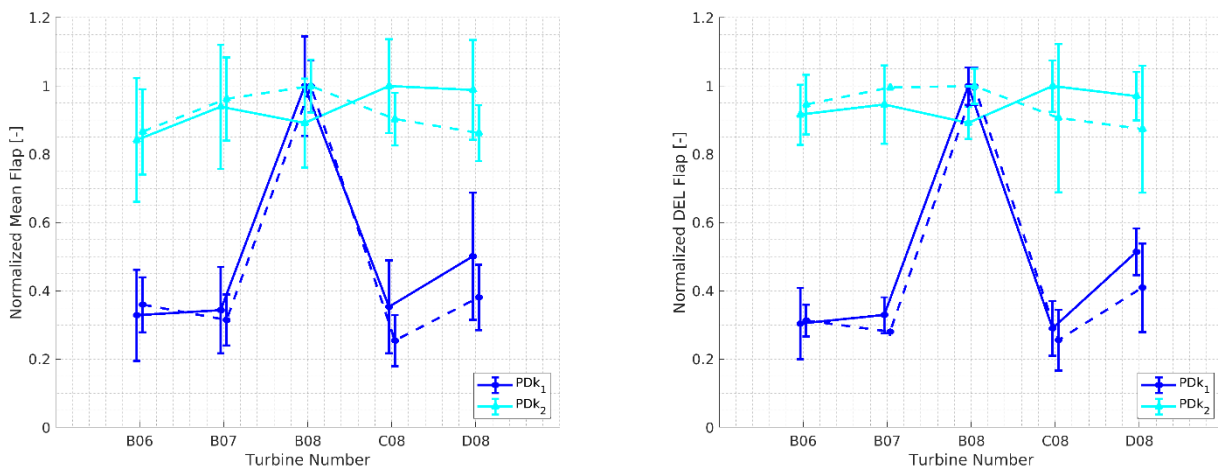


Figure 12 Comparison of EllipSys3D LES time averaged blade root flapwise moments (left) and DEL (right) against field measurements. Solid lines represent the LES data and dashed lines of the same colour represent the field data. Vertical lines represent +/- 1 sta

## C. VALIDATION OF DWM MODEL

### C.1. DWM-LIDAR COMPARISON

#### C.1.1. OVERVIEW

To meet the objective of this study, the wake information in the LiDAR Data must be collected for each time stamp and compared to the corresponding wake modelled with the SGRE internal implementation of DWM. Additional environmental conditions of the farm are collected from turbine SCADA data and used as input for the DWM model. Those environmental conditions are:

- Wind direction estimated from collective turbine orientation (considered uniform through the farm).
- Inflow wind speed estimated from front machines SCADA data.
- Inflow turbulence intensity estimated from front machines SCADA data.

The comparison between LiDAR and DWM will be carried out by comparing horizontal velocity profiles at hub height on lines placed at various distances downstream of the turbine.

The study is composed of a near wake and a far wake study. The near wake study compares 7 horizontal profiles downstream the turbine of interest, from 1 diameter to 4 diameters in steps of 0.5 diameters. The far wake study compares 8 horizontal profiles, from 4 diameters to 7.5 diameters. The inter-turbine distance on Lillgrund lies between 3.3 and 4 diameters. As westerly winds were predominant in the investigated period, only turbine Bo6 could be considered for the near wake study, whereas the far wake study considers wakes from turbines Ao6, Ao7, Do7, Do8, Co5, Co6, Co7, Do6, Do7 and Eo6.

To have a correct comparison between wake profiles of LiDAR and DWM, the DWM wind field needs to be averaged over a 10-min period. To do so, 10-min wind fields are generated, combining a freestream inflow velocity field and the sum of the meandering disturbances (velocity deficit and added turbulence) from the upstream turbines' wakes. In a first study, wake superposition is carried out according to Annex E of the IEC61400 standard (IEC, 2019). The freestream inflow properties match one-to-one the measured 10-min averaged wind speed, direction and turbulence intensity. The wind field is then averaged in time to obtain the 10 min mean wind profile.

After these steps, the data is ready to be compared. Figure 13 and Figure 14 are respectively examples for a near wake and a far wake comparison when the wind is near the rated wind speed, which is 12 m/s. In Annex, Figure 37 and Figure 48 are examples of near wake comparisons below and above the rated wind speed whereas Figure 59 and Figure 20 are examples for far wake comparisons below and above the rated wind speed. The left sub-figures show a top view of the relevant section of the Lillgrund Wind farm superimposed on the 10-minute average LiDAR wind data at hub height. The right sub-figures show the normalised streamwise wind component from LiDAR data and DWM for horizontal lines at different spacings downstream the turbine of interest

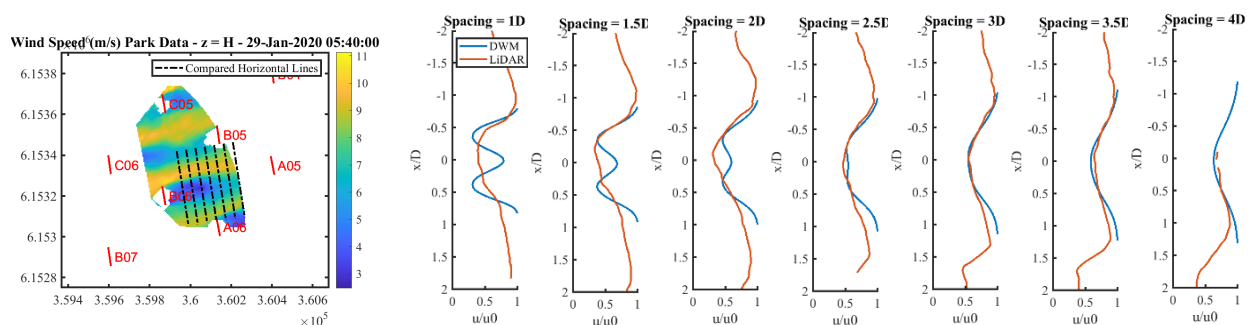


Figure 13: Example of a Near Wake comparison

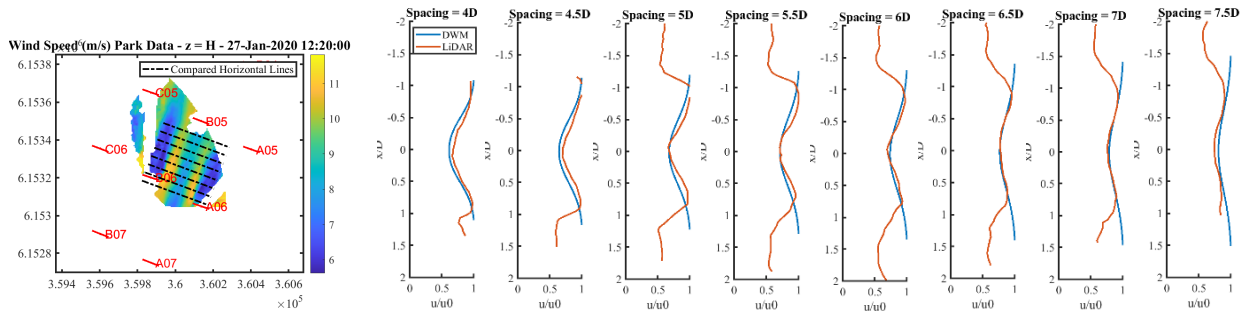


Figure 14: Example of a Far Wake comparison on A07

Close to the turbine, a stark mismatch is observed, with the DWM model showing a pronounced “double bell” shaped wake profile. This is a consequence of the “instantaneous wake expansion” employed in the DWM wake model to avoid resolving pressure-driven wake expansion (Larsen, 2007). The double bell shape reflects the thrust distribution at the rotor plane, and while observed in the LiDAR data immediately behind the rotor, results from the DWM do not exaggerate the phenomenon significantly. At downstream distances between 2 and 3 turbine diameters the double bell shapes disappear in the DWM results and a good match with LiDAR data is observed.

### C.1.2. ANALYSIS OF THE DATA

As the objective is to compare the wake deficits from the LiDAR data and the DWM model, a quantitative measure of the error is needed. In this study, the normalised RMSE is used. The wake profiles from LiDAR and DWM are interpolated onto the same points, allowing to estimate the RMSE by evaluating the difference point by point:

- Locate the area where a wake is observed in both the DWM and the LiDAR data. This will be referred as the coincident wake.
- Compute the normalised RMSE, defined as:

$$RMSE_{normalised} = \frac{1}{U_{undisturbed}} \sqrt{\frac{1}{N} \sum (U_{LiDAR} - U_{DWM})^2}$$

where

$N$  is the number of discrete points within the coincident wake limits

$U_{undisturbed}$  is the wind speed not influenced by any wake, the inflow wind speed

$U_{LiDAR}$  are the values of each discrete points for the LiDAR data

To find the coincident wake, there must be a definition of the wake limit. Here, the wake limit is defined when the wind speed returns to 95% of the maximum wind speed left and right of the wake respectively. The normalised RMSE is calculated at all spacings and all timesteps.

As this measure of the error is defined positive and because of inevitable noise in the measured data (both LiDAR and inflow conditions) the normalised RMSE cannot be expected to reach 0%. Therefore, a limit of 10% for the normalised RMSE is defined to say DWM could be confidently used to model the wake.

### C.1.3. RESULTS

The wake deficits of the LiDAR data and the DWM model have been compared by computing the normalised RMSE on a discrete range of turbine spacings for all exploitable data collected in the last week of January 2020. A near-wake study on turbine Bo6 and a far-wake study on all exploitable data was carried out. The number of exploitable time steps varies for each spacing, ranging from 150 up to 500. Figure 15 represents the average normalized RMSE for each spacing. DWM has been used as described in Annex E of the IEC61400 standard (IEC, 2019). Local conditions for all turbines are computed from the undisturbed conditions, wind direction and farm data considering the presence of wakes. This process is essentially the same as that used to derive the 10-min averaged DWM wind field described above, with a final integration of the wind properties over the rotor plain. Moreover, when the wind speed is below the rated wind speed, only the most influencing turbine (the wake-inducing turbine) is considered in the computation of the deficit. This method will be referred in the results as the *Standard* method.

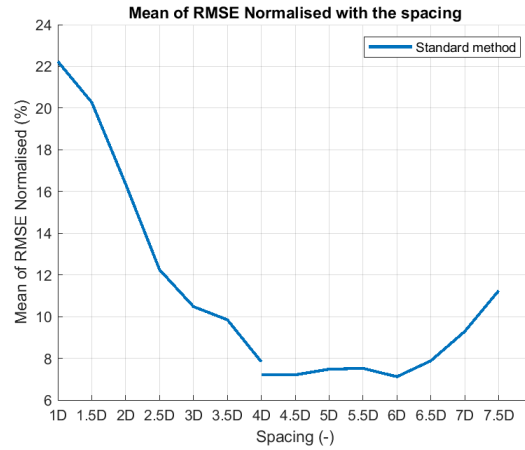


Figure 15: Mean of standard RMSE for the Standard method

As mentioned, the near wake study (1 diameter to 4 diameters) only concerns the turbine Bo6, whereas the far wake study combines various target turbines. Consequently, there is no continuity at 4D in the results. As can be seen in Figure 15, the mean of normalised RMSE is decreasing with the spacing. The high mean RMSE at the closest spacings can be explained by the double bell form of the DWM model. As the double bell form vanishes for higher spacings results improve rapidly, with a RMSE reaching close to 10% at 3 diameters and going below this limit at 3.5 diameters. From 6 diameters to 7.5 diameters, the mean of the normalised RMSE is increasing. This might be explained by the fact that there are less exploitable datapoints, with extreme errors among them that have a strong influence on the mean value.

As the study has been done according to the standard and its superposition, the rest of the study will compare it with another assumption on the superposition.

## C.2. A NEW APPROACH OF DWM

### C.2.1. AN ALTERNATIVE WAKE SUPERPOSITION ASSUMPTION

With the *Standard* method, when the wind speed is below the rated wind speed, only the most influencing turbine (the wake-inducing turbine) is considered in the computation of the deficit.

In this study, another way to use DWM has been tried. This time, all turbines are considered for the computation of the deficit at all wind speeds. This method will be referred as the *Standard All* method.

### C.2.2. RESULTS

The same study as before has been launched with the two different methods and the results are presented in the Figure 26.

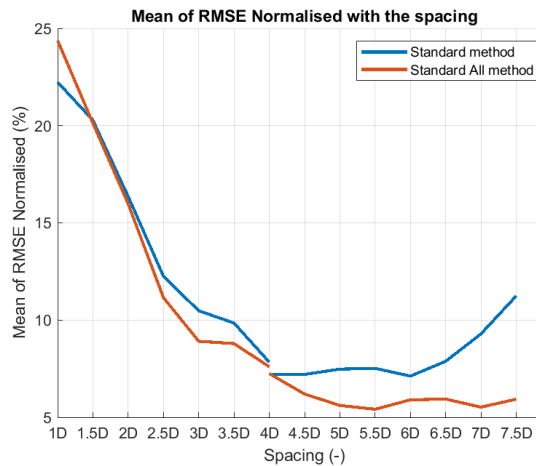


Figure 26: Mean of standard RMSE for the two methods

Again, the mean of normalised RMSE is decreasing quickly with the spacing. Yet, from 2.5 to 7.5 diameters, using the *Standard All* method gives a normalised RMSE which is 2 to 5% lower than with the *Standard* method. Therefore, the

10% limit is reached between 2.5 and 3 diameters for the *Standard All* method instead of 3.5 diameters. Moreover, there are no extreme values which are disturbing the mean from 6 to 7.5 diameters. Therefore, considering all wakes at all wind speeds leads to improved and more stable wake deficit results for the DWM model.

### C.2.3. CONCLUSION

Data from the Lillgrund LiDAR campaign constitutes a unique opportunity to validate the DWM model against actual wind field measurements in the presence of wakes. Using this dataset, this study has shown that model results for the wake profile attain a reasonable error level starting from an inter-turbine distance of 3 to 3.5 diameters. Changing the superposition assumptions to include wakes from all turbines at all wind speeds improves results compared to the superposition assumptions prescribed by the IEC51400 standard, suggesting this might be a better approach for the DWM wake model. To confirm this assumption, load studies should be carried out comparing the two approaches.

As the 10% limit has been arbitrarily set, a load study could also bring clarity on the usability of the DWM wake model at 3 to 3.5 diameters, both for the *Standard* and *Standard All* methods. From the current results, and considering the defined threshold on the normalized RMSE, we can state that the *Standard* method can be used down to 3.5 diameters, with 3 diameters being very much on the limit (11%). The *Standard All* method improves results and brings the error below 10% starting from 2.5 diameters. However, the uncertainty in the data remained high despite careful filtering, and the analysed time period is limited. Future studies on an extended dataset as well as load studies could be envisioned to refine the statement.

## D. CONCLUSIONS AND DISCUSSION

The application for numerical models to simulate flows in offshore wind farms has a great potential in understanding and improving the operation of large wind farms. In this work, three numerical solvers are used to recreate the conditions measured at the Lillgrund offshore wind farm through a measurement campaign, which provided a comprehensive validation dataset comprising of inflow, SCADA, loading and wake measurements. Two high-fidelity LES solvers, SP-Wind (KU Leuven) and EllipSys-3D (DTU), are used to conduct aeroelastic simulations through the entire wind-farm, while a low-fidelity solver, DWM (Siemens) is used to conduct a comparison of the turbine wakes in a smaller section of the wind farm where wake measurements were available.

While all three models were able to successfully recreate the inflow conditions at the Lillgrund wind farm based on LiDAR and SCADA measurements, the reported results highlight their respective strengths and weaknesses:

SP-Wind was generally able to predict the power prediction and mean-flapwise loading for the majority of the wind farm, however higher errors were observed when comparing some of the turbines operating in a waked state. This could be a result of not using a sufficiently fine grid resolution, which would be able to better capture the wake effects. Another source of error is attributed to the differences in the controller implemented in the simulation domain due to lack of full knowledge of the field controller, as well as the assumption that all the turbines face the free-stream wind direction, leading to yaw misalignment errors.

EllipSys-3D is also generally able to capture the inflow conditions, turbine power and loading trends across the wind farm, however larger differences are observed in the power production when compared to the results from SP-Wind. Results from a refined simulation have been included, which showed a decrease in the power production, as expected. The discrepancies can be due to differences in the simulated inflow, unintentional yaw misalignment and/or controllers. It is unclear why the predictions of EllipSys3D deviates more from the measurements than SP-Wind, but is most likely due to differences in the rotor force smearing and tip correction method. However, the normalized load estimates from EllipSys-3D match the measurements very well as numerical results and measurements always overlap each other within one standard deviation.

DWM is focused on simulating the wakes of the turbines, hence power and loading comparison was not possible against the other solvers. However, when comparing turbine wakes and recovery, DWM is able to better capture the far wake region start 3D downstream distance from the turbine, while the opposite is true for SP-Wind, which exhibited a better comparison in the near wake region and higher errors in the far wake region.

Based on the results, future work can be focused on improving the controller and turbine implementations in LES, by obtaining more detailed information about the controllers from the farm operators and using a refined grid. A study could also be conducted on the different tip smearing models used in the two different LES solvers to evaluate the impact on the comparison. In the DWM, load studies could be carried out to compare the two wake superposition methods discussed in this work.

## E. REFERENCES

- Allaerts, D., Meyers, J., 2015. Large eddy simulation of a large wind-turbine array in a conventionally neutral atmospheric boundary layer. *Phys. Fluids* 27. <https://doi.org/10.1063/1.4922339>
- Anderson, S.J., Meyers, J., Sood, I., Troldborg, N., 2020. TotalControl D 1.04 Flow Database for reference wind farms.
- Castro, I.P., 2007. Rough-wall boundary layers: Mean flow universality. *J. Fluid Mech.* 585, 469–485. <https://doi.org/10.1017/S0022112007006921>
- Freebury, G., Musial, W., 2000. Determining equivalent damage loading for full-scale wind turbine blade fatigue tests. 2000 ASME Wind Energy Symp. 287–297. <https://doi.org/10.2514/6.2000-50>
- Goit, J.P., Meyers, J., 2015. Optimal control of energy extraction in wind-farm boundary layers. *J. Fluid Mech.* 768, 5–50. <https://doi.org/10.1017/jfm.2015.70>
- Jiménez, J., 2004. Turbulent flows over rough walls. *Annu. Rev. Fluid Mech.* 36, 173–196. <https://doi.org/10.1146/annurev.fluid.36.050802.122103>
- Martinez-Tossas, L.A., Churchfield, M., Leonardi, S. Large eddy simulations of the flow past wind turbines: actuator line and disk modeling. *Wind Energy*, 2015; 18:1047:1060. DOI: 10.1002/we.1747
- Munters, W., Meneveau, C., Meyers, J., 2016. Turbulent Inflow Precursor Method with Time-Varying Direction for Large-Eddy Simulations and Applications to Wind Farms. *Boundary-Layer Meteorol.* 159, 305–328. <https://doi.org/10.1007/s10546-016-0127-z>
- Munters, W., Meyers, J., 2018. Dynamic strategies for yaw and induction control of wind farms based on large-eddy simulation and optimization. *Energies* 11. <https://doi.org/10.3390/en11010177>
- Socie, D.F., Downing, S.D., 1982. Simple Rainflow Counting Algorithms. *Int. J. Fatigue* 4, 31–40.
- Sutherland, 1999. Fatigue analysis of wind turbines. Technical report, Sandia National Laboratories.
- Townsend, 1976. *The Structure of Turbulent Shear Flow*. Cambridge University Press.
- Vitsas, A., Meyers, J., 2016. Multiscale aeroelastic simulations of large wind farms in the atmospheric boundary layer. *J. Phys. Conf. Ser.* 753, 082020. <https://doi.org/10.1088/1742-6596/753/8/082020>

# ANNEX

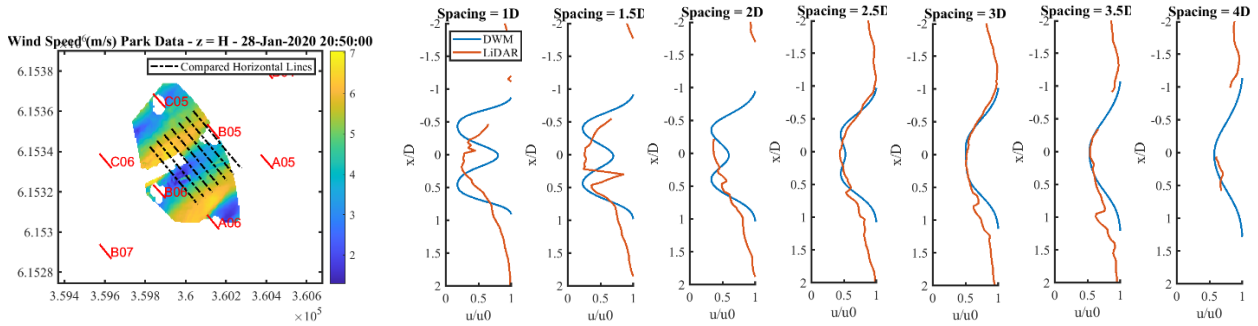


Figure 37: Near Wake comparison for a wind speed below the rated wind speed

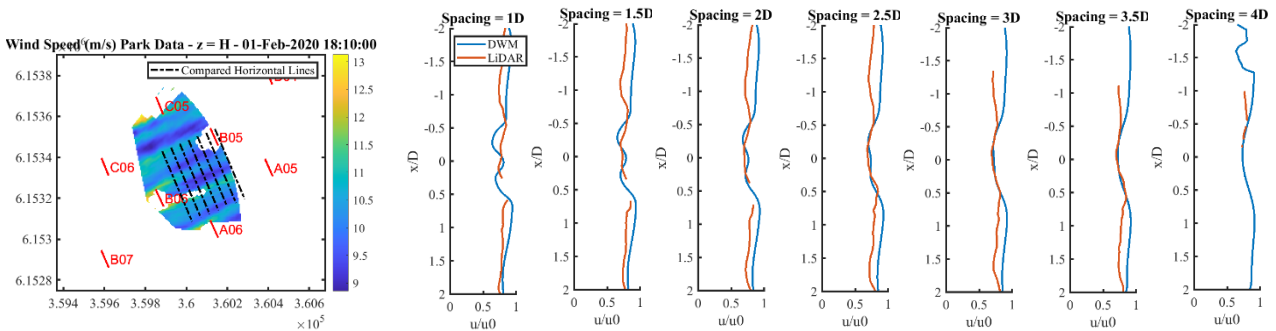


Figure 48: Near Wake comparison for a wind speed above the rated wind speed

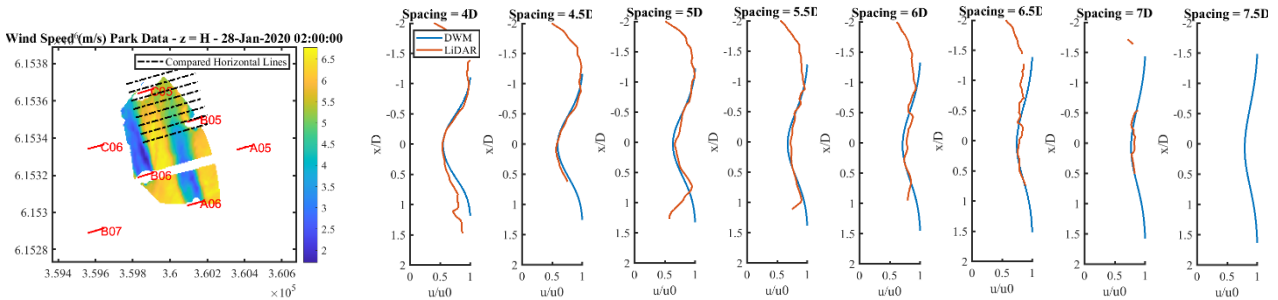


Figure 59: Far Wake comparison for a wind speed below the rated wind speed on turbine Ao6

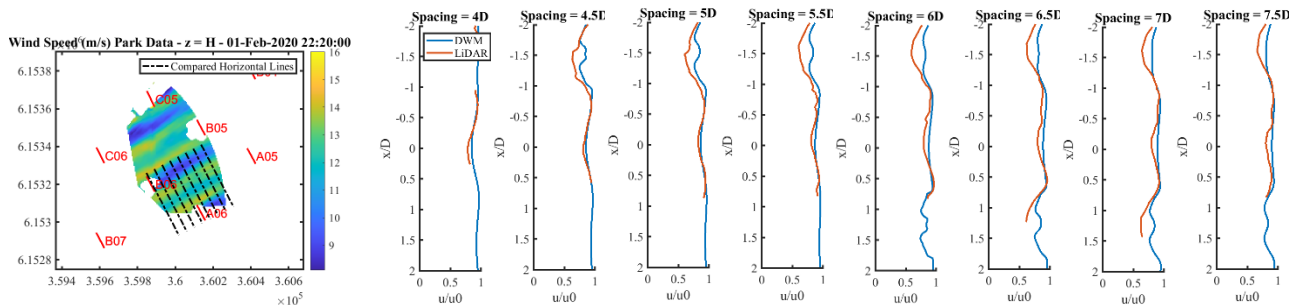


Figure 20: Far Wake comparison for a wind speed above the rated wind speed on turbine Bo7